

IGNITABILITY AND MIXING OF UNDEREXPANDED HYDROGEN JETS

Ruggles, A.J. and Ekoto, I.W.

Sandia National Laboratories, Livermore, CA 94551-0969, USA, ajruggl@sandia.gov

ABSTRACT

Reliable methods are needed to predict ignition boundaries that result from compressed hydrogen bulk storage leaks without complex modelling or experimentation. To support the development of these methods, a new high-pressure stagnation chamber has been integrated into Sandia National Laboratories' Turbulent Combustion Laboratory so that relevant compressed gas release scenarios can be replicated. For the present study, a jet with a 10:1 pressure ratio issuing from a small 0.75 mm radius nozzle has been examined. Jet exit shock structure was imaged by schlieren photography, while quantitative Planar Laser Rayleigh Scatter imaging was used to measure instantaneous hydrogen mole fractions downstream of the Mach disk. Measured concentration statistics and ignitable boundary predictions compared favourably to analytic reconstructions of downstream jet dispersion behaviour. Model results were produced from subsonic jet dispersion models and by invoking self similarity jet scaling arguments with length scaling by experimentally measured effective source radii. Similar far field reconstructions that relied on various notional nozzle models to account for complex jet exit shock phenomena failed to satisfactorily predict the experimental findings. These results indicate further notional nozzle refinement is needed to improve the prediction fidelity. Moreover, further investigation is required to understand the effect of different pressure ratios on measured virtual origins used in the jet dispersion model.

1.0 INTRODUCTION

Due to the rapid growth of hydrogen as an alternative fuel, particularly within the material handling sector, significant infrastructure upgrades are needed to accommodate the increased demand for transport to, storage of, and delivery from compressed gas bulk container systems. A prerequisite for large-scale infrastructure development is the implementation of science based safety codes and standards that rely on effective quantitative risk analysis (QRA) tools. Validated consequence models for planned and unintended hydrogen release ignitable boundaries are a necessary QRA requirement needed to establish suitable separation distances and risk mitigation features. Research into natural gas turbulent jet ignition has led to the development of the flammability factor (FF) concept, which is the integration of the conditional mole fraction probability density function (PDF) between the fuel flammability limits, and has been found to be an accurate predictor of ignition probability [1-3]. The advantage of the FF is that it can be easily modelled using mole fraction statistics that are readily determined from application of well known jet similarity arguments [4-7], provided an appropriate jet intermittency model is used [8]. Schefer et al. [9] verified the FF concept is similarly applicable for hydrogen releases from un-choked jets.

For releases where the storage pressure is above the critical ratio (~ 1.9 for hydrogen), however, the exit flow chokes and an underexpanded jet forms that is characterized by a complex shock structure and a non-uniform velocity distribution. A Mach disk, which serves as the boundary between the supersonic and subsonic portions of the jet, forms at the end of the underexpanded jet, and is often several factors wider than the jet exit diameter depending on the pressure ratio. Furthermore, elevated near field Mach numbers and entropy changes across shocks may result in jet temperature deviations from ambient. Notional nozzle (or pseudo source) models [4, 10-13] have been used to account for the jet exit shock structure by predicting effective nozzle radii and thermodynamic state variables. Downstream from the effective Mach disk, traditional subsonic dispersion models have been employed to reconstruct the mean and fluctuating scalar fields. An example is Birch et al. [12] where the dispersion model of Chen and Rodi [14] has been modified to include a modelled term that represents the effective nozzle radius, which was based upon the pressure ratio. Ignition probabilities

were then represented by FF values computed from the reconstructed scalar statistics. Agreement between the various notional models, however, is poor and limited validation data of necessary downstream concentration statistics currently exists for general heterogeneous underexpanded jets, with none available for hydrogen.

For the present study, downstream concentration statistics from an underexpanded hydrogen jet with a nominal 10:1 pressure ratio and 0.75 mm jet exit radius have been collected using Planar Laser Raleigh Scatter (PLRS) imaging. Jet exit shock structure was qualitatively imaged using schlieren photography. These data allow a direct comparison of observed jet behaviour and ignition boundaries against incompressible model predictions of dispersion statistics and ignition probabilities with notional nozzle models used to account for jet exit boundary conditions.

2.0 EXPERIMENTAL DESCRIPTION

To create the desired underexpanded hydrogen jets, a new high-pressure stagnation chamber capable of operating at pressure ratios of up to 60:1 has been designed and integrated within Sandia/CA's Turbulent Combustion Laboratory burner facility. The chamber, illustrated in Figure 1, is 345 mm long and $\text{\O}127$ mm in diameter, with 12.7 mm thick walls and a 1.24 liter internal volume. To produce a uniform stagnation flow field, fuel gas was fed from below through a six-hole injector with $\text{\O}3$ mm diameter holes evenly spaced around the circumference and angled 45° downwards from the chamber centre axis. Easily interchangeable nozzles with machined profiles were manufactured from blanks that were then securely attached to a Swagelok one inch VCO fitting (SS-16-VCO-1-16) at the chamber outlet and sealed using its o-ring. Long Radius nozzle profiles from ASME MFC-3M-2004 were selected over a simple orifice since they tend to produce fairly uniform (top-hat) velocity profiles at the nozzle exit [15] and the pressure ratios required to generate an underexpanded jet were lower for a given exit diameter [16]. Chamber temperature and pressure were respectively monitored via a type K thermocouple and TESCOM series 100 pressure transducer. Dynamic feedback was used to maintain a steady pressure ratio. The entire assembly was mounted onto a computer controlled traverse capable of movement in three dimensions, while data acquisition and system control were handled via a custom written LabView virtual instrument (VI).

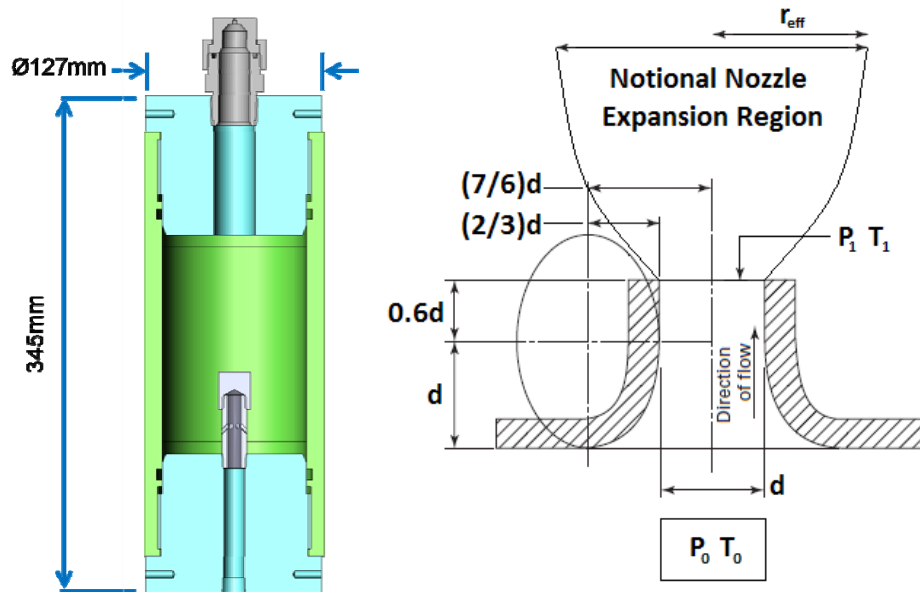


Figure 1. Left: Sectional view of the stagnation chamber and nozzle assembly. Right: Illustration of nozzle profile and Notional nozzle concept.

2.1 Jet conditions

For this work, a hydrogen jet with a 10:1 pressure ratio (stagnation to ambient pressure) was investigated using a nozzle with a 0.75 mm radius. Stagnation density, ρ_0 , was calculated from the stagnation temperature, T_0 , pressure, P_0 , hydrogen molar mass, M_F , and universal gas constant, R , using the Abel-Nobel equation of state, where an excluded volume constant, b , ($7.6921 \times 10^{-3} \text{ m}^3/\text{kg}$ [17]) was used to account for real gas compressibility effects.

$$\rho_0 = \frac{P_0}{P_0 b + T_0 (R/M_F)} \quad (1)$$

Modified isentropic relationships that incorporate the Able-Noble equation of state were used to determine static density, temperature, choked flow velocity, and mass flow rate at the nozzle exit [17]. The 0.979 discharge coefficient was determined from the nozzle exit Reynolds number and relations obtained from ASME MFC-3M-2004 [15] for the selected nozzle profile. Atmospheric laboratory pressure and temperature were 98.37 kPa and 296 K respectively. Mean conditions and respective fluctuations during data collection are summarized below in Table 1.

Table 1. Experimental conditions

	Stagnation Chamber Mean (rms)	Nozzle exit Mean (rms)
Pressure (kPa)	983.2 (3)	515.4 (1.4)
Temperature (K)	295.4 (0.4)	244.8 (0.3)
Density (kg/m ³)	0.796 (0.003)	0.504 (0.002)
Velocity (m/s)		1202.7 (0.8)
Mass Flow Rate (g/s)		1.0 (0.003)

3.0 SHOCK STRUCTURE CHARACTERIZATION

3.1 Schlieren Imaging System

Jet exit shock structures were visualized by an in-line lens based schlieren imaging system using three 50.8 mm diameter lenses and a custom built light-emitting diode (LED) light source with a fixed 520 nm (green) wavelength so that chromatic aberrations were removed. The LED light was condensed to a point by an f1.2 NIKON 50 mm camera lens, while a diffuser and iris were mounted at the focal point to create a point light source. The first field lens (plano convex $f=250$ mm) was positioned at the focal length to collimate the light. The second field lens (plano convex $f=500$ mm) then focused the light to a point at which a horizontally orientated razor blade was positioned to control the amount of light cutoff. Finally a third lens was used to focus the light onto the imaging array of a Princeton Instruments PIXIS 400B camera. A close up view was obtained through the use of a plano convex lens of $f=350$ mm and a more global view was acquired with a plano convex lens of $f=150$ mm.

Each recorded instantaneous image, $R(x,y)$, was corrected by subtraction of the electronic bias image, $E_B(x,y)$, and background image (associated with the exposure time), $B_G(x,y)$. To determine the schlieren system optical response, $O_R(x,y)$, 100 images were recorded with no nozzle flow (pure air images). Electronic bias and background scatter were corrected from each image, the images were averaged together, and the mean image was divided by the mean pixel value within the image field of view. The final corrected image, $I(x,y)$, was obtained after normalization by the optical response. The data reduction algorithm is expressed mathematically in equation 2 as:

$$I(x, y) = \frac{R(x, y) - E_B(x, y) - B_G(x, y)}{O_R(x, y)} \quad (2)$$

3.2 Results

Mean images derived from corrected schlieren images are shown in Figure 2. Typical underexpanded jet shock structures are exhibited, including the barrel shock, Mach disk, outer compression waves, and the diamond shaped reflected shock structure downstream of the Mach disk. The measured Mach disk diameter was 1.30 mm and was located 3.05 mm downstream from the nozzle exit.

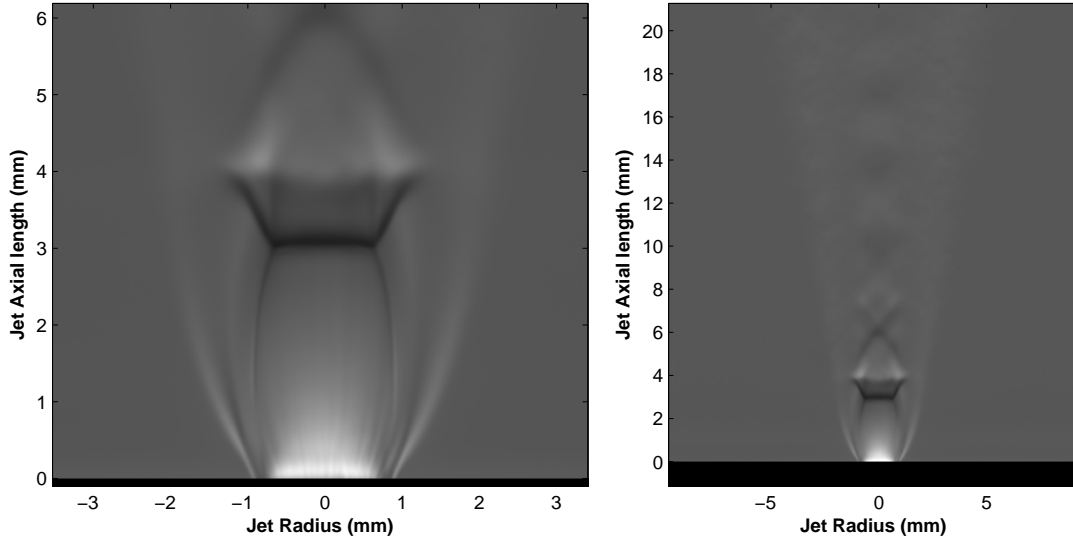


Figure 2. Left: Mean image of the Mach disk structure. Right: Mean image of the Mach disk and diamond shock structure.

For analytic predictions of jet dispersion behaviour, the effect of the complex shock structure were accounted for by 5 separate notional nozzle models that calculated effective source radii and jet exit density. All models were modified to account for compressibility effects by incorporating an Abel-Nobel equation of state into the derivation as previously done by Schefer et al. [17] using the Birch et al. model [12]. Model complexity was impacted by the assumptions made, with early models only accounting for mass conservation [4, 10], while later models successively incorporated momentum conservation [12], energy conservation [11], and the entropy change across the Mach disk [13]. A more thorough review of each model is given by Perret et al. [18]. Model results for the present operating condition are shown in Table 2, and demonstrate a large spread in model predictions with no clear agreement for either the effective source radius or density.

Table 2. Table of boundary conditions using various notional nozzle models

Model	Effective nozzle radius (mm)	Jet Density (kg/m ³)
(1) Birch et al. (1984)	1.80	0.0805
(2) Ewan and Moodie (1986)	1.70	0.0971
(3) Yüceil and Ötügen (2002)	1.15	0.1391
(4) Birch et al. (1987)	1.50	0.0805
(5) Harstad and Bellan (2006)	2.70	0.0837

4.0 SCALAR FIELD MEASUREMENTS

4.1 Planar Laser Rayleigh Scattering (PLRS) system

Since elastically scattered light is linearly proportional to the scattering cross section of the gas in question [7, 19-21], Planar Laser Rayleigh Scatter (PLRS) imaging was used to measure instantaneous mole fractions within the isothermal portion of the jet far field. Thermocouple measurements were used to find the location where the centreline jet temperature returned to within 1°C of room temperature. This point was approximately 80 mm downstream of the nozzle exit and marks the upstream limit for the Rayleigh measurements. At each position 400 images were recorded. A beam from a Nd:YAG laser (9 ns pulse duration 1 J/pulse) operating at 532 nm was formed into an approximately 40 mm high laser sheet using a cylindrical plano-concave ($f = -200$ mm) and spherical plano-convex ($f = 1000$ mm) lens pair. Five imaging areas were sampled, starting at the 80 mm downstream location, with successive areas imaged by traversing the chamber downwards in 40 mm increments. To reduce unwanted scatter, the laser and sheet forming optics were encased within a light tight enclosure that terminated close to the experimental apparatus. Once the laser sheet had passed through the test section, the light was directed into a second, narrow, enclosure with a built-in beam dump to minimize back scatter. A Princeton Instruments PIXIS 400B camera was mounted perpendicular to the laser sheet and used an f1.2 NIKON 50 mm lens with a NIKON 3T close up lens to collect the Rayleigh scattered light. To improve signal-to-noise, 2×2 on chip binning and 3×3 Gaussian smoothing was used. The system was calibrated by imaging of two pure gases, air and helium. Using 800 image averages from these data the scattering background, $S_B(x,y)$, camera optical response, $O_R(x,y)$, and camera pixel intensity $I(x,y)$ of pure air, helium, and hydrogen were all determined.

Once the raw experimental images, $R(x,y)$, were collected, each image was subjected to a dust filtering algorithm that automatically detected and masked imaged Mie scattering from dust particles. Electronic bias, $E_B(x,y)$, and background scatter, $B_G(x,y)$ were then subtracted. Laser power fluctuations were corrected for by multiplying the entire image by a correction parameter, p_F . This parameter was obtained by sampling the first 50 columns on the image right-hand-side where only pure air was sampled and then normalizing the integrated mean value of this region by the corresponding mean from the reference air calibration image. The resultant image was divided by the optical response image and the scattering background image was then subtracted. Finally the laser sheet intensity distribution, $St(x,y)$, was accounted for by sampling the same 50 columns used to obtain the power fluctuation correction and integrating each row. A new image, $St(x,y)$, was created and all pixels in each row were equal to the mean pixel value of the corresponding row sampled. The entire image was then normalized by its own mean value. The processed image was divided by $St(x,y)$ to yield a fully corrected intensity image, $I(x,y)$.

$$I(x,y) = \frac{1}{St(x,y)} \cdot \left[\left(\frac{R(x,y) - E_B(x,y) - B_G(x,y)}{p_F \cdot O_R(x,y)} \right) - S_B(x,y) \right] \quad (3)$$

Once corrected, the image intensity was converted to mole fraction using equation 4 and the previously recorded calibration intensity values.

$$M_{H_2}(x,y) = \frac{I_{AIR}(x,y) - I(x,y)}{I_{AIR}(x,y) - I_{H_2}(x,y)} \quad (4)$$

The converted image was then discretized into 1% changes based upon a signal-to-noise analysis. An example of the original raw image and the mole fraction distribution after all corrections from equations 3 and 4 have been applied is shown in Figure 3. From the processed images, ensemble averaged mean and root-mean-square (*rms*) mole fraction turbulent statistics were computed for each

section. Complete reconstruction of turbulent data from each sectional interrogation region was performed.

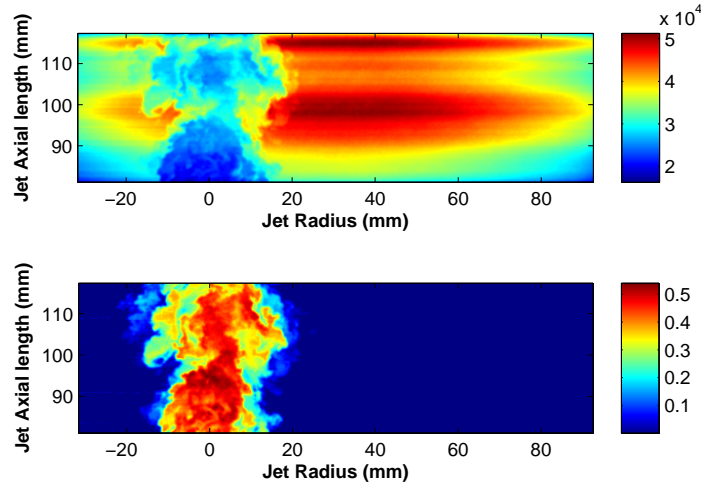


Figure 3. Top: Raw intensity image $R(x,y)$. Bottom: Corrected mole fraction image $M_{H_2}(x,y)$.

4.2 Results

To ascertain if the subsonic portion of the jet can accurately be described by conventional incompressible dispersion models, the jet was analysed to determine if it obeys jet self similarity. Images of the mean and *rms* mole fraction fields are displayed in Figure 4, and illustrate the nearly seamless sectional reconstruction.

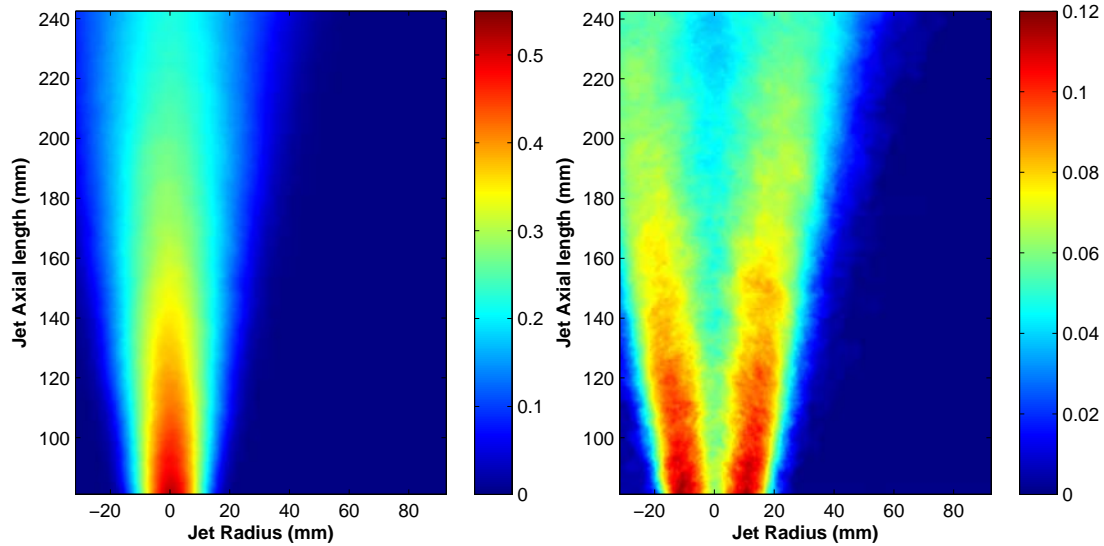


Figure 4. Left: Mean mole fraction image. Right: Rms mol fraction image

Since mass fraction statistics inherently account for momentum differences due to density effects [7], mean and *rms* mole fraction images were converted to mass fraction so that comparisons could be made with other gases. The conversion accounts for the statistical nature of the flow by including terms up to fourth order resulting in an uncertainty of much less than 1% [6]. The inverse mass fraction profile along the centreline, shown in Figure 5, confirmed the linear decay rates observed by Xiao et al. [22] and was consistent with measurements from un-choked free jets [4-7, 9]. The mass flux based virtual origin, $z_{0,y}$, or the point where the initial downstream distance of the linear inverse decay rate intercepts the axis, was found to be 24.74 mm. The jet half-width profile, derived from the mass

fraction data and also shown in Figure 5, was similarly a linear function of axial distance. The gradient of the best fit line (when plotted against axial distance) was 0.111, which is in excellent agreement with other reported values [19], although slightly larger than that reported for the hydrogen study (0.103) of Schefer et al. [20]. The momentum flux virtual origin, $z_{0,j}$, or the location where the jet half-width becomes zero was found to be 7.14 mm downstream of the nozzle exit. Both virtual origins are summarized in Table 3.

It is important to note that reported virtual origins in the present work were derived using only the subsonic concentration statistics, and thus do not explicitly account for the existence of downstream reflected shock structures that likely alter downstream centreline decay rates in the region just beyond the Mach disk. The behaviour of both virtual origins has been observed in previous investigations [19, 23-25], and general trends have been identified. For example, the momentum flux virtual origin, $z_{0,j}$, was found to have a Reynolds number dependence, with higher Reynolds numbers resulting in downstream movement of the origin as observed by Richards and Pitts [19]. The mass flux virtual origin, $z_{0,y}$, likewise moving downstream as Reynolds numbers increase [19, 24]; however, this origin also depends on the jet exit gas density, with increased values resulting in upstream movement [19, 23, 25]. To the best of the authors' knowledge, no suitable model has been proposed that predicts the position of either origin. Nonetheless, in the case of underexpanded jets where both the density and Reynolds number are large relative to unchoked releases the origin $z_{0,j}$ can be expected to move downstream. The second origin is not as straightforward since there will be competition between the increased jet exit density and higher Reynolds numbers. Although the results in Table 3 indicate both virtual origins extend several jet diameters downstream from the nozzle exit, the contribution from the downstream shock structure on the virtual origin position is unknown.

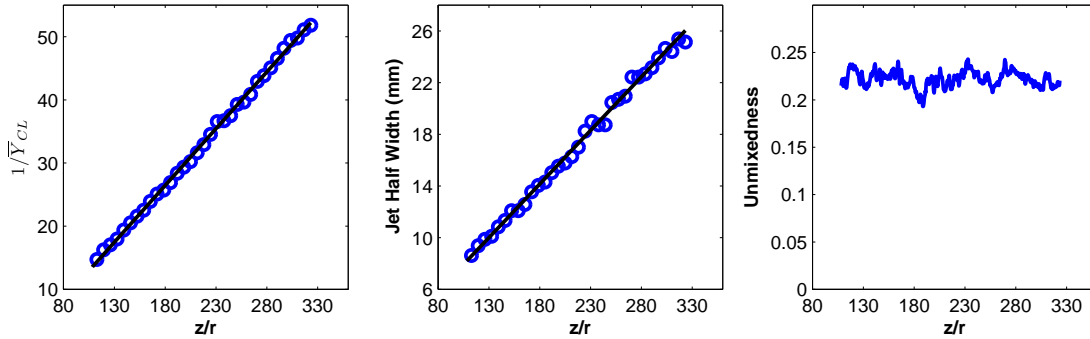


Figure 5. Left: Reciprocal mean mass fraction along the centreline. Centre: Jet half widths against normalised axial distance. Right: Centreline unmixedness.

Table 3. Summary of the mass and momentum flux virtual origins.

Virtual Origin	Length
$z_{0,y} / r$	32.0
$z_{0,j} / r$	9.52

Figure 5 also displays a profile of unmixedness, which is defined as the ratio of *rms* to mean mass fraction, and has been shown to converge to a steady asymptotic value between 0.21 and 0.24 for self preserving jets [19, 23, 25]. The measured value, 0.222 ± 0.009 , was in good agreement with these studies and further supports the assertion that downstream of the nozzle exit shock structure the jet is self similar.

5.0 JET RECONSTRUCTION

Richards and Pitts [19] have demonstrated that atmospheric jet dispersion behaviour for a variety of gases (methane, propane and helium) can be described by the following equations for the mean and *rms* fields respectively:

$$\bar{Y}(z, \eta) = \frac{9.52r_\varepsilon}{z - z_{0,Y}} \exp(-59\eta^2) \quad (5)$$

$$Y'(z, \eta) = \frac{9.52r_\varepsilon}{z - z_{0,Y}} \left[0.23 + 0.35\eta + 9.09\eta^2 - 116.48\eta^3 + 240.81\eta^4 \right] \quad (6)$$

where $\eta = r/(z - z_{0,j})$ was a nondimensional radial coordinate and $r_\varepsilon = r_0/(\rho_j/\rho_a)^{1/2}$ was a weighted nozzle radius used to account for density changes between the jet at the nozzle exit and the ambient gas (both at atmospheric pressure). Here, r_0 was the jet exit radius. A universal jet decay constant, K , ($1/K = 0.105$ when evaluating for inverse mass fraction) was used in both expressions. In addition to the present study, other researchers have found a small spread in the reported constant values among the different gases [4-7, 9]. Therefore it is common to use either a gas specific value reported from literature or the generalised one proposed by Richards and Pitts.

For the remainder of this work the above expressions will be used and compared with the collected data to judge their suitability. Schefer et al. [20], found for their atmospheric hydrogen jet that the inverse mean centreline decay constant was nearly equivalent to those of other gases (0.104). For the present work, however, the decay constant could not be independently determined as r_ε depended on an unknown effective jet exit diameter and density. Instead, r_0 and ρ_j were replaced with the effective nozzle radius, r_{eff} , and jet nozzle exit density, ρ_{eff} , derived from the notional nozzle models described in section 3.2 and tabulated in Table 2. The suitability of the values from each model was determined by computing the gradient of reciprocal mass fraction against axial distance. Equation 5 was evaluated at the centreline ($\eta = 0$), the generalized K value given by Richards and Pitts was assumed and $r_{\varepsilon,ideal}$, or the measured r_ε value, was calculated from a linear fit to the measured $1/\bar{Y}_{CL}$ values shown in Figure 5. Different values from the notional nozzle model predictions of effective radius and jet exit density are summarized in Table 4 along with a comparison of the deviation from $r_{\varepsilon,ideal}$. Most modelled values are within $\pm 10\%$; however, the differences in all cases are non-negligible.

Table 4. Table of r_ε . $r_{\varepsilon,ideal} = 0.438$ mm

Model	r_ε (mm)	$r_\varepsilon / r_{\varepsilon,ideal}$
(1) Birch et al. (1984)	0.475	1.084
(2) Ewan and Moodie (1986)	0.492	1.123
(3) Yüceil and Ötügen (2002)	0.399	0.911
(4) Birch et al. (1987)	0.396	0.904
(5) Harstad and Bellan (2006)	0.726	1.658

Measured mean and *rms* mass fractions radials are plotted as a function of η in Figure 6. Since normalized mean and *rms* data both collapse to single curves, it was concluded that the jet is self similar downstream of the Mach disk, and mass fraction statistics can be accurately described by incompressible dispersion models. The curve from equation 5 was overlaid on the data and compared with a best fit curve to the exponential constant in equation 5 ($C = -57.7$). The differences between the two fitted curves were so slight that the original formulation was assumed to hold without any loss of

prediction fidelity. It should be noted that both curves slightly overestimate the data at the tail beyond $\eta = 0.2$.

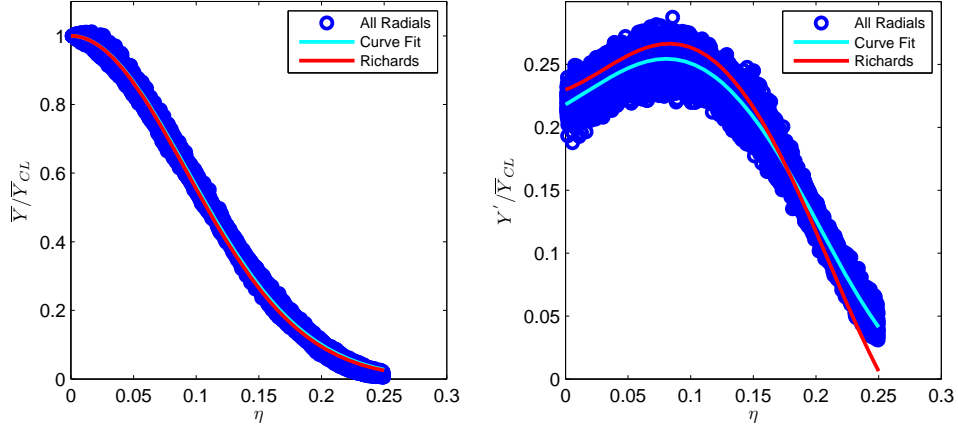


Figure 6. Left: Plot of normalised radial mass concentration including the corresponding best fit curve and equation 5 [19]. Right: plot of normalized rms radial data including the corresponding best fit curve and equation 6 [19].

The *rms* field was similarly reconstructed using equation 6, and plotted in Figure 6 as a function of η . A best fit radial curve to the measured data was matched to a 4th order polynomial and was also overlaid for comparison; the curve fit is displayed in equation 7.

$$Y'(z, \eta) = \frac{9.52r_\varepsilon}{z - z_{0,y}} \left[0.218 + 0.541\eta + 4.570\eta^2 - 86.388\eta^3 + 192.51\eta^4 \right] \quad (8)$$

The difference between the two curves was more substantial than for the mean mass fraction curve fits. The impact of the difference on ignitability predictions will be discussed further in the next section.

6.0 IGNITION PROBABILITIES

To estimate ignition probabilities the validated Flammability Factor concept (*FF*) was utilised [1, 9], which is expressed in equation 8. Here $M_{H_2}(x, y)$ corresponds to a fully corrected instantaneous mole fraction image (see Figure 3) and $n(x, y)$ the number of valid samples at each pixel. For hydrogen, the lower and upper flammability limits used were 0.04 and 0.75 respectively.

$$FF(x, y) = \sum \left(\int_{LFL}^{RFL} M_{H_2}(x, y) = 1 \right) \times \frac{1}{n(x, y)} \quad (8)$$

In Figure 7, measured *FF* contours, acquired from direct application of equation 8 to the collected instantaneous mole fraction measurements, were compared with those derived from the reconstructed mean and *rms* statistics derived from equations 5 and 7 and the intermittency model described by [8]. Although the comparison was very good for all of the contours, better agreement was obtained for higher *FF* values (i.e., 0.9) closer to the centreline, which was attributed to the slight overestimation of the mean mass fractions at large radial distances (Figure 6).

To demonstrate the utility of this approach a 10% ignitability contour was predicted in the far field with the respective effective radius and density from each notional nozzle model along with equations 5 and 6 to model dispersion characteristics. Additionally, this contour was created using the ideal $r_{e,ideal}$ values obtained from equations 5 and 6 ('Ideal (2)') or equations 5 and 7 ('Ideal') to highlight the impact of the different coefficients for the 4th order polynomial. All ignitability contours are compared in Figure 7. The maximum axial extent for both the Ideal and Ideal (2) 10% *FF* contours was

1888 mm and 1911 mm respectively; thus the impact of selecting equation 6 or 7 to model mass fraction r_{ms} values appears to be negligible. Predictions of the maximum FF axial extent by the Yüceil and Ötügen [11] and Birch et al. [12] models underestimated the contour location by around 200 mm relative to the Ideal conditions, while the Birch et al. [4] and Ewan and Moodie [10] model predictions overestimated the location by a similar spread. Although the Hardstad and Bellan model [13] has the most realistic physical basis, it vastly overestimated the 10% FF contour by more than a meter. It should be noted that this particular model, incorporating the Abel-Nobel equation of state, did not sufficiently capture the real gas effects in the cryogenic regime upstream of the Mach Disk, in particular the temperature. Predicted percentage differences in FF contour distance were proportional to the differences in r_{ϵ} values reported in Table 4.

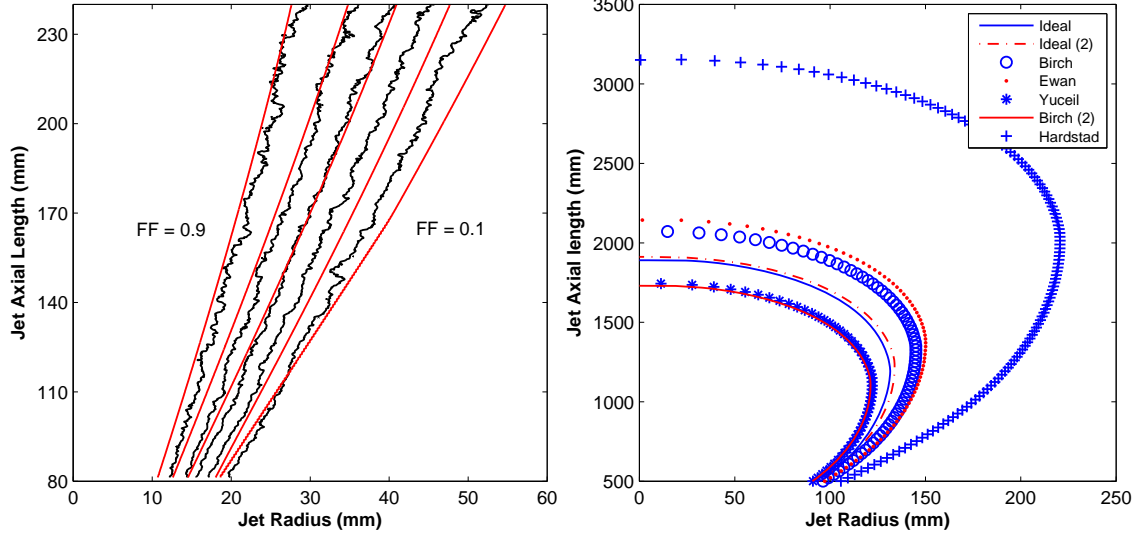


Figure 7. Left: Comparison of experimental (black) and reconstructed (red) FF contours. Right: Comparison of the 10% (0.1) FF based on notional nozzle models predictions for r_{ϵ} (Table 4), along with experimentally determined values of $r_{\epsilon,ideal}$ and r_{ms} mass fractions predicted using either equation 6 (Ideal (2)) or equation 7 (Ideal) .

It should be cautioned that these contours only correspond to the 10% probability that an ignition kernel will form. Determination of whether the ignition kernel will transition to sustained jet light-up or will be subsequently extinguished, however, is beyond current predictive capabilities of simplified engineering models. Swain et al. [26] and Schefer et al. [9] observed centreline flame light-up boundaries near the 10% mole fraction contour; however, no explanation was given for why it occurred in this region and it is possible that the agreement was serendipitous. For the present study, the centreline jet light-up position was determined using a similar laser spark ignition apparatus to that described by Schefer et al. [9]. Sparks were formed on the chamber centreline using the second harmonic of an Nd:YAG laser operating at 15 Hz with 100 mJ/pulse. The chamber slowly traversed upwards until a sustained flame was achieved. The test was repeated 10 times to ensure consistency. The average height above the nozzle where sustained combustion occurred was found to be 367 mm, which roughly correlates with the 15% mean mole fraction contour. It should be noted that a similar laser spark ignition test was performed with a 1.0 mm nozzle at the same pressure ratio and light-up was never achieved at any height. This last result agrees with Devaud et al. [27], who found that the critical diameter for hydrogen jet light-up was approximately 1 mm. These results demonstrate that neither the FF nor the mean concentration alone is sufficient to predict the downstream light-up location.

7.0 CONCLUSIONS AND FUTURE WORK

To support the development of reliable ignition boundary prediction methods for releases from compressed hydrogen bulk storage releases, a new high-pressure stagnation chamber has been designed and integrated into Sandia/CA's Turbulent Combustion Laboratory. For the present study, a hydrogen jet with a 10:1 pressure ratio that issued from a 0.75 mm radius nozzle was examined using a combination of shock imaging via schlieren photography and quantitative downstream concentration measurements by Planar Laser Rayleigh Scatter imaging. The present results demonstrate that once an underexpanded jet has returned to subsonic flow conditions downstream of the release, the scalar field follows canonical jet similarity laws and can accurately be described by empirical jet dispersion relations provided an appropriate effective source nozzle radius and density is used. Mean mass fraction statistics agreed very well with reported subsonic values in the literature, while the *rms* mass fraction field exhibited small deviations. More work is needed to ascertain if these coefficients significantly change with different pressure ratios, jet diameters or gas types.

Good agreement was observed between experimental and reconstructed ignition probability boundaries regardless of the correlation used to predict fluctuating statistics, so long as the density weighted effective radius derived from concentration decay measurements was used. Pseudo source models based on different combinations of mass, momentum, and energy conservation were used to predict density weighted effective radii, however, the results were off by $\pm 10\%$ relative to measured values. A more physically realistic source model proposed by Harstad and Bellan overestimated the density weighted effective radius by more than 60%, which suggests certain physical processes such as the thermodynamics before the shock were poorly reconstructed. Since the error in ignition probability boundaries was proportional to the error in density weighted effective radii, better source model performance is needed to improve the agreement between predictions and measurements. The present results also demonstrate that non-negligible downstream movement of the mass and momentum flux based virtual origins has occurred, and these values likewise must be accounted for.

Future models with improved thermodynamics, near field jet entrainment, and a more comprehensive account of downstream reflected shock structures are under development, and will be validated against data generated from different conditions at higher pressure ratios and different nozzle radii. Furthermore, methane will be investigated to ascertain model applicability for other flammable gases. Ultimately it should be noted that the present models are applicable only for ignition probability and further research is needed to develop the scientific underpinnings for engineering models that can accurately predict the transition to sustained flame light-up.

8.0 REFERENCES

1. Birch, A.D., Brown, D.R., Dodson, M.G., Ignition probabilities in turbulent mixing flows, Proceedings of the 18th International Symposium on Combustion, The Combustion Institute, 1981, pp. 1775-1780.
2. Birch, A.D., Brown, D.R., Cook, D.K., Hargrave, G.K., Flame Stability in Underexpanded Natural-Gas Jets, *Combust Sci Technol*, **58**, No. 4-6, 1988, pp. 267-280.
3. Birch, A.D., Brown, D.R., G., D.M., Thomas, J.R., Studies of Flammability in Turbulent Flows using Laser Raman Spectroscopy, Proceedings of the 17th International Symposium on Combustion, The Combustion Institute, 1979, pp. 307-314.
4. Birch, A.D., Brown, D.R., Dodson, M.G., Swaffield, F., The Structure and Concentration Decay of High-Pressure Jets of Natural-Gas, *Combust Sci Technol*, **36**, No. 5-6, 1984, pp. 249-261.
5. Becker, H.A., Hottel, H.C., Williams, G.C., Nozzle-Fluid Concentration Field of Round Turbulent Free Jet, *J Fluid Mech*, **30**, 1967, pp. 285-&.
6. Birch, A.D., Brown, D.R., Dodson, M.G., Thomas, J.R., Turbulent Concentration Field of a Methane Jet, *J Fluid Mech*, **88**, No. Oct, 1978, pp. 431-449.
7. Pitts, W.M., Kashiwagi, T., The Application of Laser-Induced Rayleigh Light-Scattering to the Study of Turbulent Mixing, *J Fluid Mech*, **141**, No. Apr, 1984, pp. 391-429.

8. Cho, J.R., Chung, M.K., A Kappa-Epsilon-Gamma Equation Turbulence Model, *J Fluid Mech*, **237**, 1992, pp. 301-322.
9. Schefer, R.W., Evans, G.H., Zhang, J., Ruggles, A.J., Greif, R., Ignitability limits for combustion of unintended hydrogen releases: Experimental and theoretical results, *Int J Hydrogen Energy*, **36**, 2011, pp. 2426-2435.
10. Ewan, B.C.R., Moodie, K., Structure and Velocity-Measurements in Underexpanded Jets, *Combust Sci Technol*, **45**, No. 5-6, 1986, pp. 275-288.
11. Yuceil, K.B., Otugen, M.V., Scaling parameters for underexpanded supersonic jets, *Phys Fluids*, **14**, No. 12, 2002, pp. 4206-4215.
12. Birch, A.D., Hughes, D.J., Swaffield, F., Velocity Decay of High-Pressure Jets, *Combust Sci Technol*, **52**, No. 1-3, 1987, pp. 161-171.
13. Harstad, K., Bellan, J., Global analysis and parametric dependencies for potential unintended hydrogen-fuel releases, *Combust Flame*, **144**, No. 1-2, 2006, pp. 89-102.
14. Chen, C.J., Rodi, W., Vertical turbulent bouynant jets - a review of experimental data, *The Science and Applications of Heat and Mass Transfer*: Pergamon Press, 1980.
15. Measurement of Fluid Flow in Pipes Using Orifice Nozzle and Venturi, ASME MFC-3M-2004, pp. 54.
16. Addy, A.L., Effects of Axisymmetric Sonic Nozzle Geometry on Mach Disk Characteristics, *AIAA Journal - Technical Notes*, **19**, No. 1, 1981, pp. 121-122.
17. Schefer, R.W., Houf, W.G., Williams, T.C., Bourne, B., Colton, J., Characterization of high-pressure, underexpanded hydrogen-jet flames, *Int J Hydrogen Energy*, **32**, No. 12, 2007, pp. 2081-2093.
18. Perret, C., Chaudourne, S., Pitre, C., Simulation of accidental hydrogen releases in a refuelling station. HyApproval 04-01449, CEA;
19. Richards, C.D., Pitts, W.M., Global Density Effects on the Self-Preservation Behavior of Turbulent Free Jets, *J Fluid Mech*, **254**, 1993, pp. 417-435.
20. Schefer, R.W., Houf, W.G., Williams, T.C., Investigation of small-scale unintended releases of hydrogen: momentum-dominated regime, *Int J Hydrogen Energy*, **33**, No. 21, 2008, pp. 6373-6384.
21. Schefer, R.W., Houf, W.G., Williams, T.C., Investigation of small-scale unintended releases of hydrogen: Buoyancy effects, *Int J Hydrogen Energy*, **33**, No. 17, 2008, pp. 4702-4712.
22. Xiao, J., Travis, J.R., Breitung, W., Hydrogen release from a high pressure gaseous hydrogen reservoir in case of a small leak, *Int J Hydrogen Energy*, **36**, No. 3, 2011, pp. 2545-2554.
23. Pitts, W.M., Effects of Global Density Ratio on the Centerline Mixing Behavior of Axisymmetrical Turbulent Jets, *Exp Fluids*, **11**, No. 2-3, 1991, pp. 125-134.
24. Pitts, W.M., Reynolds-Number Effects on the Mixing Behavior of Axisymmetrical Turbulent Jets, *Exp Fluids*, **11**, No. 2-3, 1991, pp. 135-141.
25. Schefer, R.W., Dibble, R.W., Mixture fraction measurements in a turbulent nonreacting propane jet, AIAA Paper 86-0278, 1986.
26. Swain, M.R., Filoso, P.A., Swain, M.N., An experimental investigation into the ignition of leaking hydrogen, *Int J Hydrogen Energy*, **32**, No. 2, 2007, pp. 287-295.
27. Devaud, C.B., Kelman, J.B., Moss, J.B., Stewart, C.D., Stability of underexpanded supersonic jet flames burning H-2-CO mixtures, *Shock Waves*, **12**, No. 3, 2002, pp. 241-249.